Hindawi
Advances in Civil Engineering
Volume 2021, Article ID 2511582, 17 pages
https://doi.org/10.1155/2021/2511582

Research Article

Fracture Modeling of the Bi-Block Ballastless Track System Resulting from Early-Aged Relative Humidity during the Construction Process

Shihao Cao[1], **Wang Hui**[2], **Shufang Zhai**[1], **Kui Hu**[1], **Yujing Chen**[1], **and Junqi Chen**[1]

[1]*College of Civil Engineering, Henan University of Technology, Zhengzhou 450001, China*
[2]*School of Civil Engineering and Architecture, Hainan University, Haikou 570228, China*

Correspondence should be addressed to Wang Hui; huiwang@hainanu.edu.cn

Received 8 September 2021; Accepted 12 October 2021; Published 25 October 2021

Academic Editor: Qinghua Zhang

Drying-induced cracks are an important issue for bi-block ballastless track system consisting of foundation, precast sleepers, and cast-in-place track slab, which not only significantly affects the comfortableness and safety of rapid transit railway but also reduces the service life of ballastless track. In order to explore its damage mechanism, this work presents an evolution model of relative humidity (RH) in the CRTS I bi-block ballastless track system by considering the actual construction sequence and environmental conditions to simulate the crack propagation induced by nonuniform RH field. Firstly, based on the node coupling technique, a three-step transfer process of RH is designed to separately investigate the influence of the construction sequence on the early humidity field in the foundation, sleepers, and cast-in-place track slab, and then the nonuniform distribution of early humidity field in the ballastless track system is determined. Subsequently, the formation mechanism of shrinkage crack in the system is analyzed, and the crack propagation path is predicted by using the mixed-mode fracture criterion. The results show that the maximum relative humidity gradient (RHG) appears at the interface between the track slab and the sleeper after concreting the cast-in-place track slab, which causes the maximum principal stress due to the drying shrinkage property of concrete materials. When the maximum principal stress exceeds the tensile strength of the interface, an interface crack will be generated and converted to a splayed crack with an initial angle of about 45° at the sleeper corner, which will be further propagated under the action of drying shrinkage deformation and finally forms a transverse through-wall crack in the track slab. The simulated crack propagation path agrees with the observed one at the site well, and thus the results are beneficial to understand the formation mechanism of through-wall crack in the track slab and further guide the construction design of the bi-block ballastless track system.

1. Introduction

Since the operation of Beijing-Tianjin intercity high speed railway in 2008, Chinese rapid transit railway has made a rapid development and remarkable achievement [1]. Ballastless track has become the main structural type of rapid transit railway because of its good stability and less maintenance. By the end of April 2021, the total mileage of rapid transit railway has reached about 38,000 kilometers in China [2, 3]. As the most widely used type of ballastless track, the CRTS (Chinese Railway Track System) I bi-block ballastless track has been applied on more than 44 rapid transit railways such as Wuhan-Guangzhou, Xi'an-Chengdu, and Lanzhou-Xinjiang lines [4]. According to the difference of structures built on the subgrade, bridge, and tunnel, the CRTS I bi-block ballastless track can be divided into three types. The schematic diagram of CRTS I bi-block ballastless track in tunnel is shown in Figure 1, which consists of rail, fastener, sleeper, track slab, and tunnel foundation [5]. However, the ballastless track, as the basis for rapid transit railway, is directly exposed to the atmosphere and eroded by the complex environment factors. These influencing factors make the component materials of the ballastless track in a continuous deterioration process [6–8]. Through the field

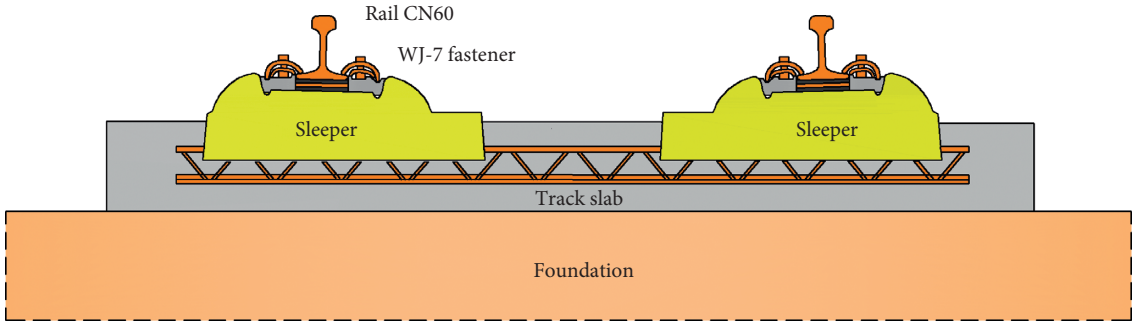

Figure 1: Diagram of CRTS I bi-block ballastless track in tunnel.

investigation, it is found that the early cracks are more likely to occur on the surface of track slab due to the bad construction and inadequate design, and then these cracks would rapidly develop into obvious water diseases in abundant rain or poor drainage areas, as shown in Figures 2(c) and 2(d).

The bi-block ballastless track has large contact area with the external environment, and thus the transport of moisture from concrete to environment is significantly affected by the environmental humidity. After concreting the track slab, the hydration of concrete materials will lead to the overall decrease of relative humidity inside the structure. Then, the higher humidity diffuses from track slab to sleepers and ambient dry air, as shown in Figure 2(b). Due to the slow transport rate of moisture in concrete materials, the nonlinear humidity gradient is formed in the ballastless track by the difference of low surface humidity and high internal humidity. On account of the wetting expansion and drying contraction of concrete materials, the shrinkage deformation and stress will occur under the nonlinear humidity gradient. Once the stress is greater than the ultimate tensile strength of concrete, the early cracks will form in the structure, as shown in Figure 2(c).

Figure 3 shows the distribution of early cracks on the track slab of bi-block ballastless track, which was discovered during the investigation of a new bi-block ballastless track. Combined with existing reports [9], the characteristics of cracks on the track slab of bi-block ballastless track can be described as follows: (1) the majority of cracks occurred at the age of 2~3 days or 2 months after the initial setting of track slab; (2) the splayed crack first appeared at the corner of sleeper, and its initial angle is about 40°; (3) the crack angle decreases with the propagation of crack and gradually tends to 0°; (4) the cracks at corner of adjacent sleepers would be coalesced and finally form a transverse through-wall crack in the track slab. Currently, the formation mechanism of early drying-induced cracks on the track slab is not clear.

In view of the causes of early cracks in the ballastless track, Wang [9] firstly conducted a statistical analysis of the early crack characteristics on the track slab under construction and pointed out that the temperature and drying shrinkage deformation could be the main reasons for the early cracks. Over the next decade, the related researches [10, 11] mainly focus on the strength and stability caused by temperature load and seldom consider the influence of shrinkage deformation resulting from internal relative humidity. Based on the heat-moisture-deformation coupling analysis, Chen [12] found that the shrinkage deformation of concrete with a 1% drop in humidity is equivalent to a 2°C drop in temperature. The research results of Li et al. [4] and Yang et al. [6] indicate that the maximum humidity gradient on the surface of the concrete in a dry environment is dozens of times the temperature gradient. That is, the drying shrinkage deformation is much greater than the temperature deformation. Han et al. [13] believe that the contribution of drying shrinkage deformation to early crack can reach 80%. In the control of early-age cracks of track slab, the addition of anticrack steel bars can reduce the early splayed cracks, while the film-forming moisture curing can effectively reduce the irregular cracks [14]. The crack resistance test of concrete slab indicates that adding the 6% TK-ICM anticrack materials in cementitious materials can maintain the internal humidity of concrete for a long time and reduce the risk of cracking [15].

As a main component material of ballastless track, the influence of water on concrete is first reflected in its internal moisture distribution. At present, the moisture transfer model based on Fick's law is widely used to describe the moisture exchange between concrete and environment [16]. Liu et al. [17] used the finite difference method to conduct the concrete humidity. By programming the finite element program, Akika et al. [18] analyzed the humidity field of solid structure with a simplified boundary. In the aspect of experimental research, Parrott [19] fitted the formula for calculating the humidity field in a unilateral drying condition based on experimental data. Combining the theoretical and test results, Gao [20] proposed a calculation model for the concrete humidity field under dry-wet cycles. For the problem of humidity distribution in complex environment, Wang et al. [21] qualitatively analyzed the problem of parameter values affecting the calculation accuracy of humidity field. Subsequently, Gao and Wei [22] put forward the quantitative analysis method of humidity gradient in concrete slab by comprehensively considering the influencing factors such as water/cement ratio, ambient air humidity, and moisture diffusion property of concrete material. To predict the relative humidity of early-age concrete under sealed and unsealed conditions, the models for early-age relative humidity are proposed in consideration of water/cement ratio, critical time, and age of concrete [23]. In view

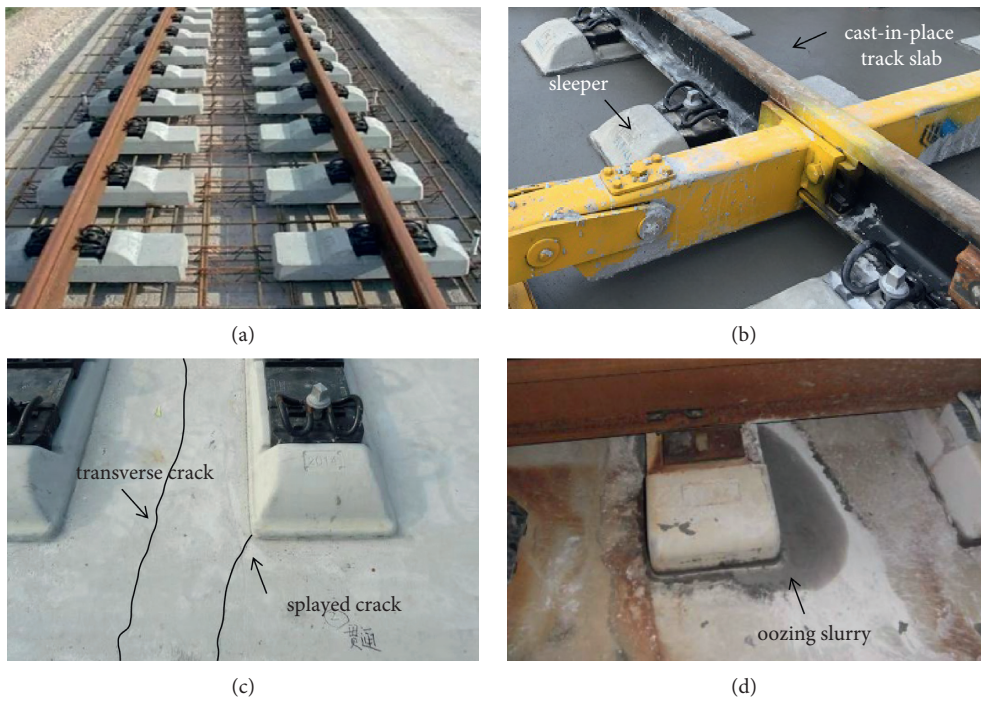

Figure 2: State of bi-block ballastless track at different stages. (a) Accurately adjusted and positioned sleepers [4]. (b) Cast-in-place track slab. (c) Early cracks. (d) Oozing slurry.

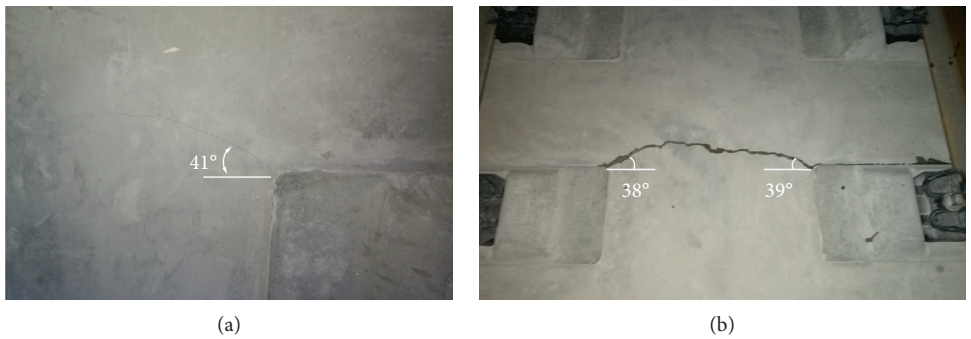

Figure 3: Distribution of cracks on the surface of track slab. (a) Initial crack. (b) Crack coalescence.

of the disadvantages of the complex numerical calculation method of humidity field which is not conducive to engineering application, Wang et al. [24] proposed a conventional method to calculate the concrete humidity field based on the temperature field module by comparing the differential equation, initial and boundary conditions of the temperature, and humidity fields. Although the scholars have studied the distribution characteristics of humidity field in concrete materials, these research results can neither consider the influence of construction characteristics of ballastless track on humidity field nor satisfy the complex humidity environment acting on ballastless track. Up to now, there are few reports on the research of early humidity field of ballastless track. To realize the early humidity analysis of the bi-block ballastless track, the following obstacles need to be resolved firstly: (1) after concreting the track slab, the three separated layers of bi-block ballastless track bond to adjacent layers, (2) affected by the construction sequence, the initial humidity field of each layer is inconsistent, and (3) the initial humidity conditions of sleepers and foundation are unknown. Therefore, the early humidity prediction presents a considerable challenge when construction sequence is taken into consideration.

In this paper, a finite element computational model of humidity distribution in ballastless track was established by introducing the complex environmental influence and construction process. Based on the node coupling technique, a three-step calculation process including one steady-state and two transient analyses was designed to realize the influence of the construction sequence on the early humidity field. Then according to the construction sequence, the early humidity field of each layer of bi-block ballastless track was analyzed, and the effects of controlling parameters related to external ambient air drying, internal hydration self-

desiccation, and local wetting time on early humidity distribution in ballastless track were analyzed. The distribution characteristics and development law of early humidity field of bi-block ballastless track were defined. Moreover, the formation mechanism of shrinkage crack was analyzed on the basis of strength theory, and the crack propagation path was predicted by using the mixed-mode fracture criterion. The research results can provide theoretical basis for optimizing track structure design and improving track construction technology.

2. Computational Model of Humidity Field in Concrete

In the complex environment, the internal relative humidity field of the ballastless track is in a state of dynamic equilibrium under the combined action of wetting on the bottom, moisture exchange between the exposed surface and the ambient air, internal moisture diffusion from high humidity region to low humidity region, and self-desiccation due to hydration of cement. To serve the practical analysis of the ballastless track, here the computational theory of humidity field is firstly reviewed.

Assuming that the RH at the position (x, y, z) and time t is $H(x, y, z, t)$, the moisture change within a closed domain Ω caused by the RH variation from $H(x, y, z, t_1)$ to $H(x, y, z, t_2)$ is

$$Q_1 = \int_{t_1}^{t_2} \left[\iiint_{\Omega} \frac{\partial H}{\partial t} \mathrm{d}V \right] \mathrm{d}t. \tag{1}$$

Considering the effect of self-desiccation of material, the moisture change from time t_1 to t_2 is

$$Q_2 = -\int_{t_1}^{t_2} \left[\iiint_{\Omega} G(x, y, z, t) \mathrm{d}V \right] \mathrm{d}t, \tag{2}$$

where $G(x, y, z, t)$ is the function of hydration self-desiccation of material, and the relationship between the hydration self-desiccation and the water-cement ratio w/c can be described as follows [24]:

$$G(t) = \frac{0.002 \cdot \exp[-(w/c)/0.3068]}{(1 + 0.43t)^{1.2}}. \tag{3}$$

The moisture in the structure will diffuse from high humidity region to low humidity region under the action of humidity gradient, and the moisture diffused through a tiny surface is proportional to the time dt, surface area dA, and humidity gradient along the surface normal direction; that is,

$$\mathrm{d}Q_3 = -D(x, y, z, t) \frac{\partial H}{\partial n} \mathrm{d}A\mathrm{d}t, \tag{4}$$

where $\partial H/\partial n$ is the change rate of humidity along the normal direction of surface and $D(x, y, z, t)$ is the coefficient of moisture diffusion which is a function of the internal RH [22]:

$$D(H) = D_1 \left[\alpha + \frac{1 - \alpha}{1 + \left(1 - H/1 - H_c\right)^{\beta}} \right]. \tag{5}$$

In equation (5), D_1 is the maximum moisture diffusion coefficient, α is the ratio of minimum to maximum moisture diffusion coefficient, H_c is the relative humidity when $D(H) = 0.5D_1$, and β is the material constant.

Therefore, the total amount of water diffused through the closed surface from time t_1 to t_2 can be written as

$$Q_3 = \int_{t_1}^{t_2} \left[\iiint_{\Omega} D\nabla^2 H \mathrm{d}V \right] \mathrm{d}t. \tag{6}$$

According to the law of conservation of mass, $Q_1 = Q_2 + Q_3$, we have

$$\int_{t_1}^{t_2} \left[\iiint_{\Omega} \frac{\partial H}{\partial t} \mathrm{d}V \right] \mathrm{d}t = -\int_{t_1}^{t_2} \left[\iiint_{\Omega} G(x, y, z, t) \mathrm{d}V \right] \mathrm{d}t + \int_{t_1}^{t_2} \left[\iiint_{\Omega} D\nabla^2 H \mathrm{d}V \right] \mathrm{d}t. \tag{7}$$

The humidity boundary condition for the ballastless track can be divided into the following two categories.

(1) The humidity on the material surface is a known function related to time; that is,

$$H_m = H(t). \tag{8}$$

(2) The moisture exchange coefficient between the exposed surface and ambient air is known; then,

$$-D \frac{\partial H}{\partial n} = a_m \left(H_m - H_s\right), \tag{9}$$

where H_s is the RH of the ambient air, H_m is the RH of the exposed surface, and a_m is the moisture exchange coefficient.

In order to verify the correctness of the computation model of concrete early humidity field, a concrete specimen from casting to curing stage is considered, as shown in Figure 4. A serial of monitoring points A, B, C, D, and E were set in the calculation model, and the corresponding distance to the upper surface is 2, 8, 15, 25, and 28 cm, respectively. The calculation conditions were set as follows: within 28 days after casting the concrete specimen, the upper surface of specimen is exposed to the ambient air with a RH of 65%. After this, the bottom is in contact with water directly.

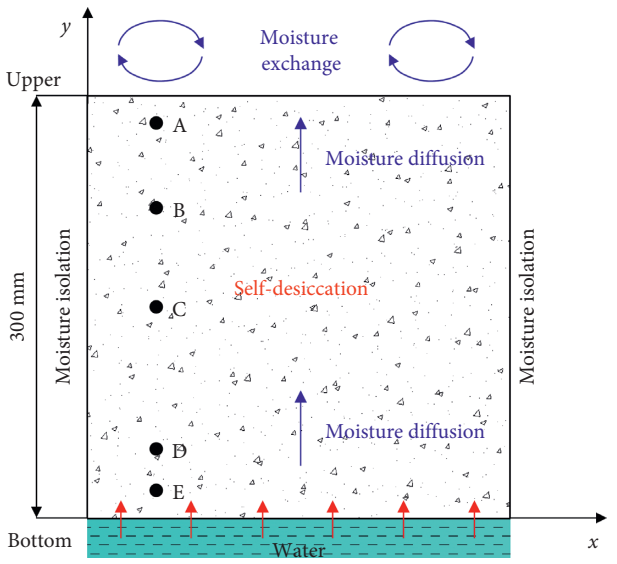

Figure 4: Early humidity field calculation model of concrete specimen ($w/c = 0.4$).

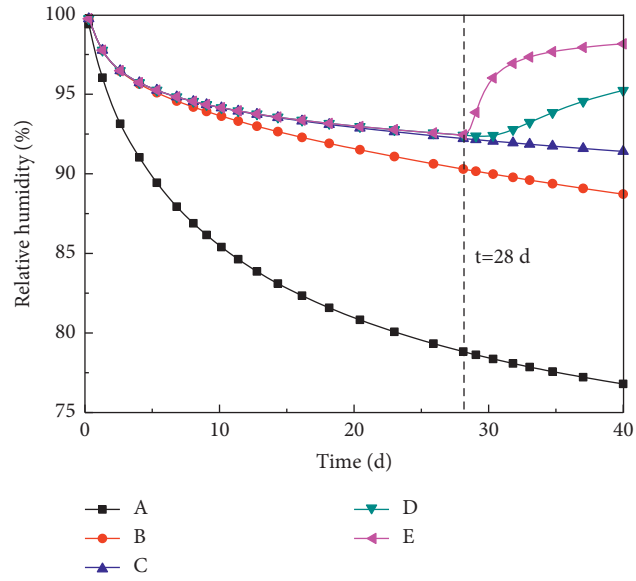

Figure 5: Variations of RH at different monitoring points.

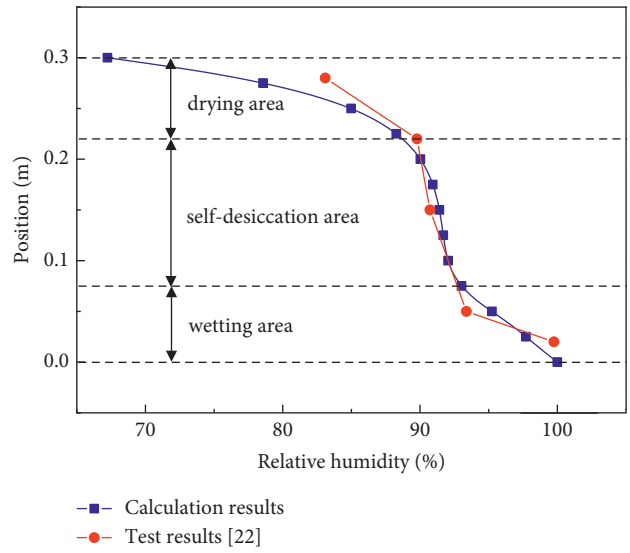

Figure 6: RH distribution along the vertical direction ($t = 40$ d).

Furthermore, both the left and right sides of the concrete specimen keep isolated from the ambient air. Using ANSYS Workbench 18.0, the concrete specimen is discretized by 900 elements. The resulting humidity distribution in the specimen is shown in Figures 5 and 6.

As can be seen from Figure 5, since the monitoring point A is close to the upper surface and greatly affected by the dry ambient air, the relative humidity declines rapidly over time. For the deeper monitoring point B and below, due to the slow rate of moisture diffusion in the concrete material, the declining rate and amplitude of humidity are significantly smaller than those at monitoring point A, and the humidity reduction is mainly caused by the hydration self-desiccation. At the age of 28 days, the specimen bottom is beginning to contact with the water directly, and the relative humidity of monitoring points adjacent to the bottom increases to a different degree. Due to the fast rate of capillary water absorption, the relative humidity at monitoring point E increases rapidly, while the relative humidity at monitoring point D increases with a delay amplitude and slow rate but still shows a rising trend. From Figures 6 and 7, it can be seen that, under the combined action of upper drying air, bottom wetting environment, and internal hydration self-desiccation, the moisture variation in the concrete specimen can be divided into three regions along depth: (1) the influence area of the ambient drying air is about 8 cm away from the upper surface; (2) the influence area of the wetting environment is within 7.5 cm from the bottom; (3) the influence area of hydration self-desiccation is the intermediate region with a uniform humidity distribution. In addition, the numerical calculation value of relative humidity is in good agreement with the test result, so it can be considered that the transient calculation model of humidity field established in this paper can be used to predict the humidity distribution of ballastless track under the complex environment.

3. Early Humidity Field Calculation Model and Process of Ballastless Track

3.1. Calculation Model. In this paper, the CRTS I bi-block ballastless track in tunnel is focused on to establish the humidity field calculation model, as shown in Figure 8. The model consists of bi-block sleepers (800 mm × 140 mm × 300 mm), track slab (2800 mm × 260 mm × 6250 mm), and foundation (5800 mm × 2000 mm × 6250 mm). The corresponding material parameters are shown in Table 1 [20, 22, 25]. In order to solve the unsteady moisture diffusion problem, the internal moisture source with negative value is used to control the hydration self-desiccation of early-age concrete, as shown in equation (3). Meanwhile, the convective moisture flux is applied on the exterior boundaries of ballastless track to realize the moisture

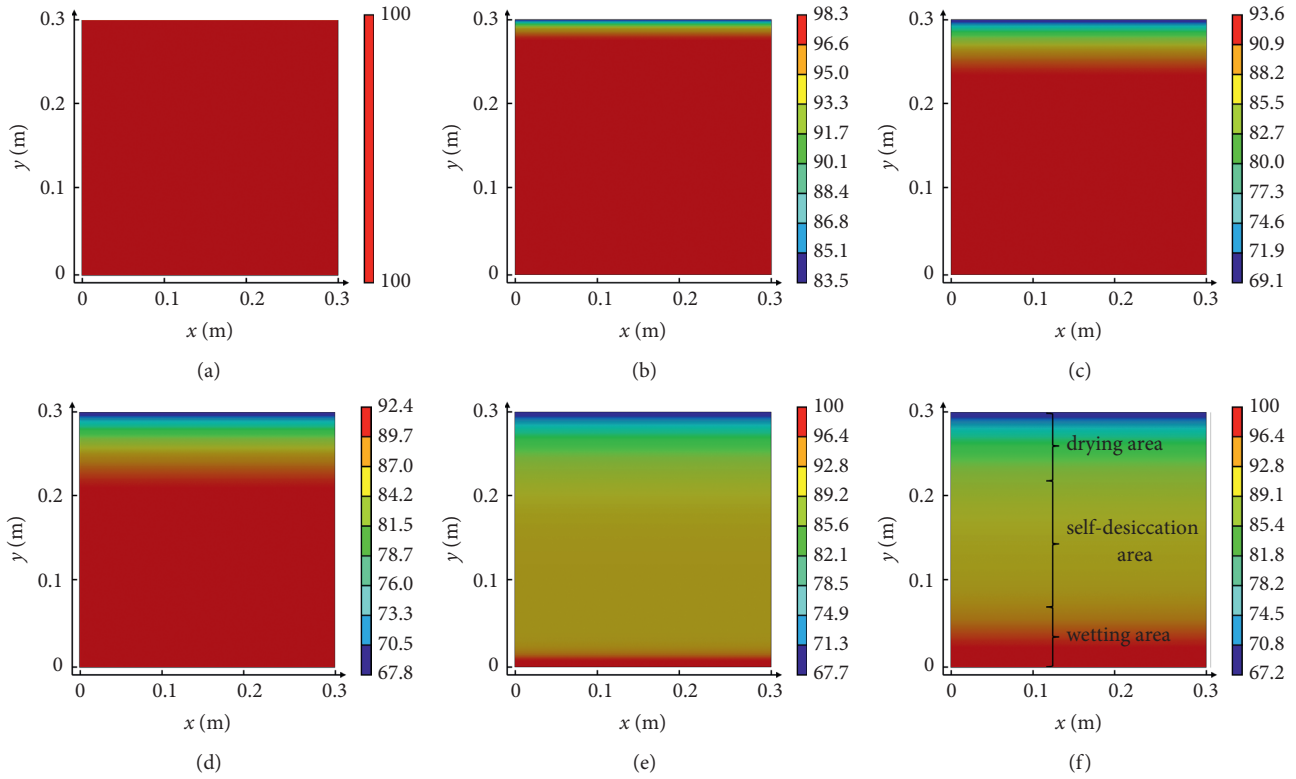

Figure 7: RH contour of concrete specimen at different times. (a) $t = 0$ d, (b) $t = 1$ d, (c) $t = 14$ d, (d) $t = 28$ d, (e) $t = 29$ d, and (f) $t = 40$ d.

exchange between exterior boundaries and ambient air. The external ambient relative humidity is set to be 65%, and the moisture transfer coefficient a_m is listed in Table 1. In addition, the wet boundary is specified as constant relative humidity of 100%.

3.2. Calculation Process. CRTS I bi-block ballastless track is a kind of track structure which is one-time cast-in-place after assembling the prefabricated bi-block sleepers into track panels. It is important to notice that the three separated layers of bi-block ballastless track will be bonded to adjacent layer after concreting the track slab. Meanwhile, the initial humidity conditions of three layers are nonuniform and inconsistent. In order to overcome the above technical obstacles, based on the node coupling technique, the three-step calculation process including one steady-state and two transient analyses was designed to realize the influence of the construction sequence on the early humidity field, as shown in Figure 9.

(1) Step 1: Under the long-term action of groundwater infiltration and external ambient air drying, the humidity field of foundation is in equilibrium. First, the steady humidity field of foundation is obtained by conducting a steady-state humidity field analysis. This steady result will be used as the initial humidity condition of foundation for the transient humidity field analysis of ballastless track in step 3.

(2) Step 2: The sleepers are precast at the factory and maintained to $t = 60$ d. In this case, their humidity distribution is mainly affected by the external ambient air drying and internal hydration self-desiccation. In this step, the variation of humidity field is obtained by carrying out a transient humidity field analysis of sleepers. The last-time result is used as the initial humidity condition of sleepers for the transient humidity field analysis of ballastless track in step 3.

(3) Step 3: To control the interface state transition before and after concreting the track slab, the node coupling technique is applied at the interfaces between track slab and sleepers, track slab and foundation, as shown in Figure 10. Before concreting the track slab, the node coupling technique is deactivated, and the interface state keeps separated. After concreting the track slab, the node coupling technique is activated, and the interface state translates from separated state to bonded state. Then, the initial high humidity will diffuse from track slab to sleepers and foundation through the bonded interfaces.

According to the above calculation process, the early humidity distribution characteristics of CRTS I bi-block ballastless track can be defined. The initial conditions, boundary conditions, and result analysis of the above three steps are described in detail in Section 4.

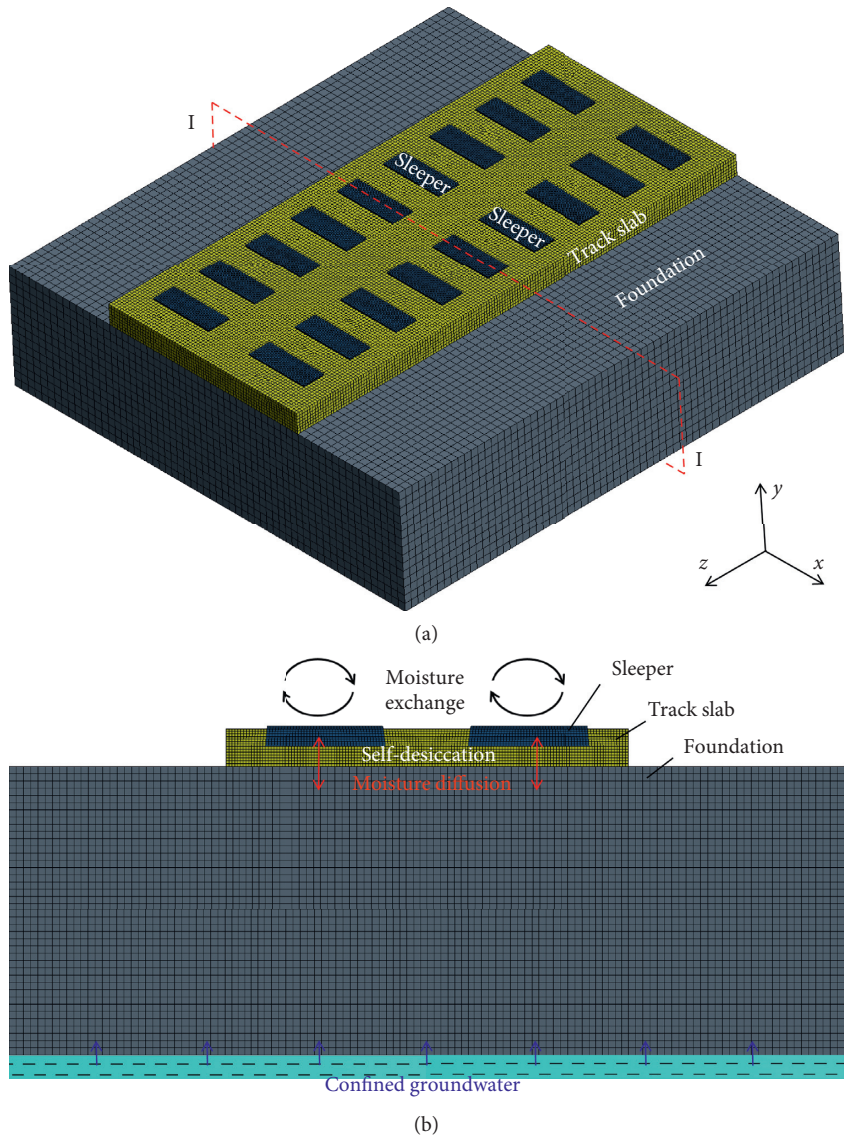

Figure 8: Early humidity field calculation model of CRTS I bi-block ballastless track. (a) Overall FE model and (b) local schematic for the cross section I-I.

Table 1: Material parameters.

Component	E_{28} (GPa)	ν	w/c	f_t (MPa)	$D_1 \times 10^{-10}$ ($m^2.s^{-1}$)	α	β	H_c (%)	a_m ($m.d^{-1}$)
Sleeper	36.0	0.2	0.3	1.54	0.25	0.018	1.3	98	0.0038
Track slab	32.5	0.2	0.4	2.39	0.5	0.022	1.1	98	0.0055
Foundation	25.5	0.2	0.6	2.74	2.02	0.071	0.8	98	0.0105

4. Early Humidity Analysis in the Ballastless Track

4.1. Steady-State Humidity Analysis of Foundation. In the tunnel, it is assumed that the groundwater exists at a depth of 2 m, and the relative humidity of the ambient air is 65%. Under the long-term action of groundwater and ambient air, the steady humidity distribution of tunnel foundation was calculated by steady-state analysis, as shown in Figures 11 and 12.

Up to now, the linear interpolation is still a common approach used to deal with the initial conditions of substructures such as tunnel foundation and subgrade bed during a transient physical field analysis of ballastless track [26]. However, in view of the nonlinear relationship between moisture diffusivity and humidity, the steady humidity distribution along the depth follows a cubic polynomial, as shown in Figures 11 and 12. The relative humidity of the upper surface is about 65.1%, which is very close to that of the ambient air in tunnel. At the depth of 1 m, the maximum

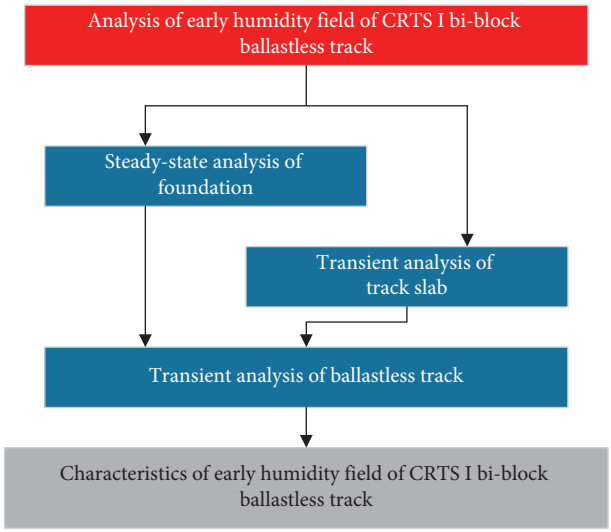

Figure 9: Early humidity field calculation process of CRTS I bi-block ballastless track.

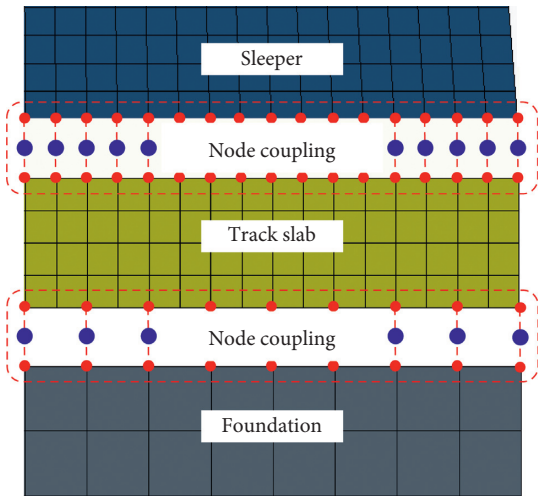

Figure 10: Node coupling technique applied at the interfaces.

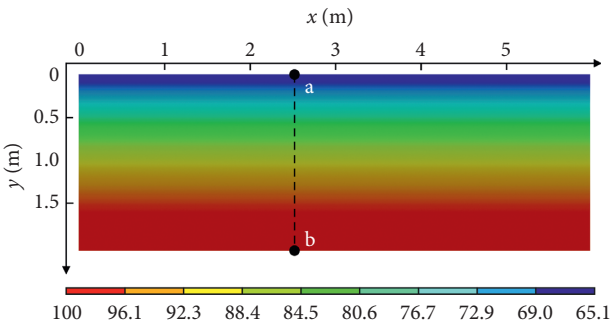

Figure 11: Steady RH contour of foundation.

difference between numerical result and linear interpolation is 7.5%. Therefore, the steady-state humidity analysis of foundation is essential, and the steady result will be as the initial humidity condition of foundation for the transient humidity field analysis of ballastless track in Section 4.3.

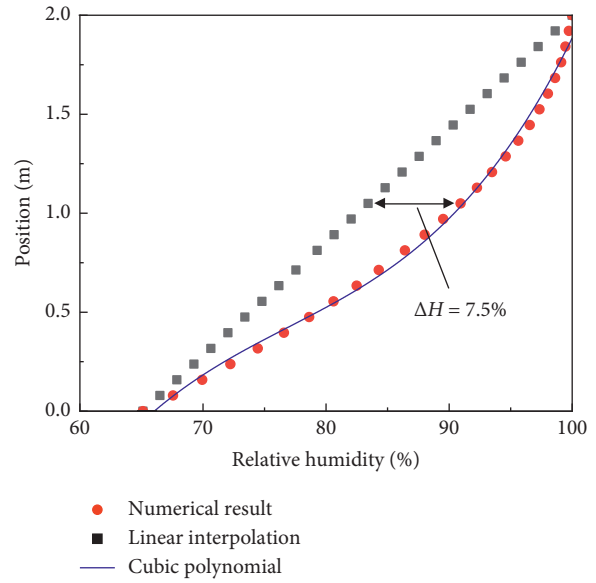

Figure 12: Distribution of RH along the path ab.

4.2. Transient Humidity Analysis of Sleeper. After concreting sleepers at the factory, the sleepers were stored in the ambient air with an average RH of 65% and RH amplitude of 50%, as shown in Figure 13, and kept for 60 days. Under the action of external ambient air drying and internal hydration self-desiccation, the humidity distribution of sleeper was calculated, as shown in Figures 14–16.

Figure 14 shows that, under the coupling effect of external air drying and internal hydration self-desiccation, the relative humidity in the sleeper shows a steady decline. On the 60th day after the sleepers have been precast, the surface relative humidity decreases to 66.6%, and the intermediate relative humidity decreases to 80.1%. The relative humidity of the surface layer of the sleeper is mainly affected by the ambient air, while the interior of the sleeper is mainly controlled by hydration self-desiccation. In order to further study the distribution of sleeper's relative humidity, the relative humidity and relative humidity gradient (RHG) along line ab shown in Figure 14(b) were calculated, as shown in Figures 15 and 16, respectively.

According to Figures 15 and 16, it is found that the typical nonlinear relative humidity gradient is formed inside the sleeper due to the slow transfer of moisture in concrete materials, which can also be approximated by a five-segment linear distribution. As a result of diurnal fluctuations of ambient relative humidity, the maximum relative humidity gradient appears around 6 mm beneath the surface of sleeper, and the limit influence depth of diurnal fluctuations of ambient relative humidity is about 8 mm. In this section, the last-time transient result will be as the initial humidity condition of sleepers for the transient humidity field analysis of ballastless track in Section 4.3.

4.3. Transient Humidity Analysis of Ballastless Track. Sixty days after the sleepers had been precast, the sleepers were transported to the construction site. Then, the track slab was poured after the sleepers had been assembled into

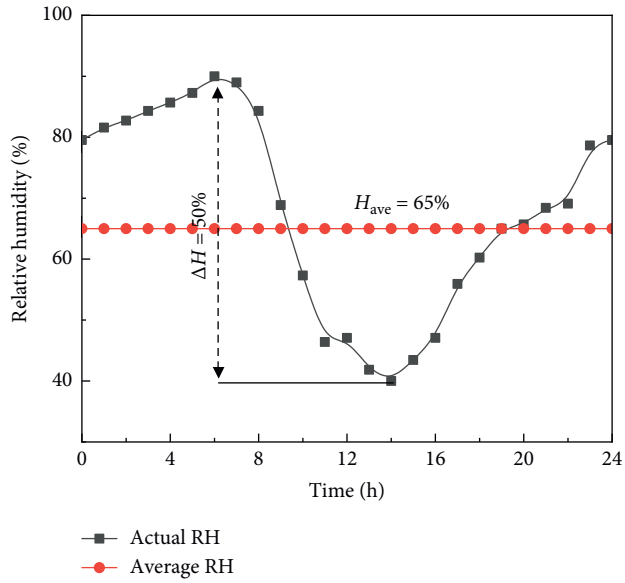

Figure 13: Daily periodic fluctuations of ambient relative humidity applied on the surface of sleeper.

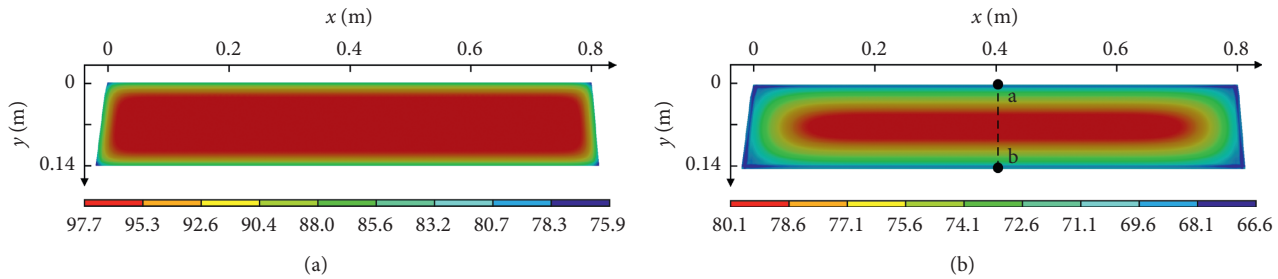

Figure 14: RH contour of sleeper at different times. (a) $t = 1$ d and (b) $t = 60$ d.

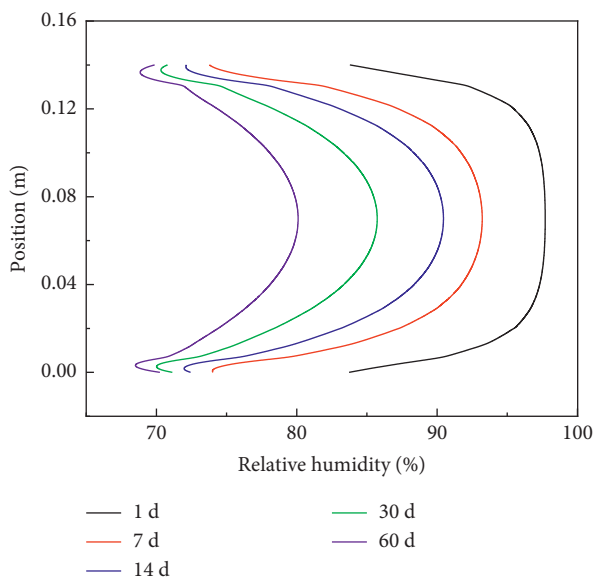

Figure 15: Distribution of RH along the path ab.

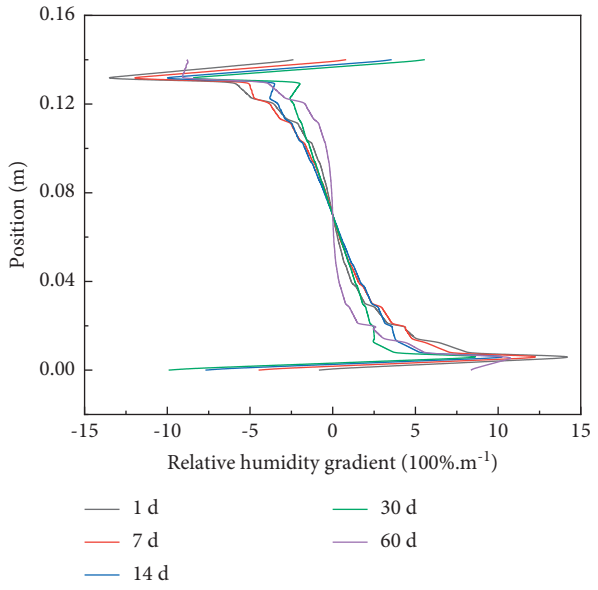

Figure 16: Distribution of RHG along the path ab.

track panels and maintained for 90 days. In this transient analysis, the initial humidity state of ballastless track is shown in Figures 17(a) and 17(b). The initial humidity of foundation used the steady-state result in Section 4.1, the initial humidity of track slab was set to be 100%, and the initial humidity of sleepers adopted the transient result in Section 4.2. In the first seven days, the exposed surfaces of ballastless track were specified as wet boundaries ($H = 100\%$) according to the construction requirements and replaced by a convective moisture flux condition ($H = 65\%$) in the days that followed. Under the water wetting, external ambient air drying, and internal hydration self-desiccation, the humidity distribution of the ballastless track was calculated, as shown in Figure 17.

It can be seen from Figure 17 that, at the initial phase after concreting the track slab, the significant difference of humidity forms on both sides of the interface. Under the driving action of humidity difference, the moisture in the structure diffuses from high humidity to low humidity areas and forms a higher relative humidity gradient at the interface, as shown in Figures 17(c), and 17(d). Subsequently, the relative humidity field inside the whole ballastless track gradually becomes stable under the continuous effect of moisture diffusion, as shown in Figures 17(c), 17(e), and 17(g). Finally, the maximum relative humidity gradient of each region appears at the surface interface, shown as points A and B in Figure 17(h). In order to further study the humidity distribution at the interface, the relative humidity and relative humidity gradient along the line ab shown in Figure 17(h) were calculated, as shown in Figures 18 and 19. Interface 1 represents the interface between sleeper and track slab, and interface 2 represents the interface between track slab and foundation.

From Figures 18 and 19, a large relative humidity gradient will occur at the interface between track slab and sleeper or the track slab and foundation. On the 1st, 3rd, 7th, 14th, 30th, 45th, 60th, and 90th days after concreting the track slab, the relative humidity gradients at the interface between the track slab and sleeper are 24.46, 14.45, 8.69, 4.17, 2.26, 1.65, 1.39, and $1.09 \times 100\%$/m, respectively. The results show that the relative humidity gradient decreases rapidly in the first week after concreting the track slab, and then the descending rate tends to be slow over time.

5. Crack Formation

5.1. Cracking Criterion. Due to the apparent characteristics of wetting expansion and drying contraction of concrete materials, the cracks in concrete structures may be caused by the nonuniform internal relative humidity. Based on the beam warping test, the relation between drying-induced strain ε and internal relative humidity H in concrete can be written as follows [27]:

$$\varepsilon = 8.14 \times (1 - H) \times 10^{-4}, \tag{10}$$

from which it is found that the nonuniform RH field leads to the nonuniform strain and then stress.

Besides, as a key parameter that affects the deformation of material, the elastic modulus of concrete increases with age, and the increase rate in early age is higher than that in the later age. In this paper, the constant elastic modulus E_{28} of sleeper and foundation listed in Table 1 is adopted, and the elastic modulus of track slab is described by exponential formula [28]:

$$E(t) = E_{28} \times \left[1 - \exp\left(-0.4t^{0.34}\right)\right], \tag{11}$$

where t is the time in day and E_{28} is the elastic modulus of the concrete at the equivalent age of 28 days.

For brittle materials such as concrete, its failure is mainly caused by the maximum tensile stress. The cracking risk of concrete can be defined as the ratio of the maximum principal stress to the tensile strength [29]; that is,

$$\zeta = \frac{\sigma_{1,\max}}{f_t}, \tag{12}$$

where ζ is the cracking risk, $\sigma_{1,\max}$ is the maximum principal stress, and f_t is the tensile strength.

Considering the fluctuating characteristics of the mechanical properties of concrete materials, it is generally believed that the crack will be caused when the cracking risk reaches 0.7 [30].

5.2. Results and Analysis. After concreting the track slab, the distributions of maximum principal stress at different times were calculated without taking into account wet curing, as shown in Figure 20.

It can be seen from Figure 20 that, in the curing stage of track slab, a certain tensile stress will be generated due to the drying shrinkage property of concrete materials, and the stresses that occur at the interface between sleeper and track slab are greater than those at other areas. When the stress exceeds the tensile strength of the interface, the interface crack will be generated.

After the interface crack between sleeper and track slab has been generated, shown as white lines ab and cd in Figure 20(b), the released energy of interface crack will be transferred to the corner of sleeper and intensifies the stress concentration effect. When the maximum principal stress exceeds the tensile strength of the track slab, the splayed crack with an initial angle of about 45° will be generated at the sleeper corner. Finally, the cracks at corner of adjacent sleepers would be coalesced and form a transverse through-wall crack of track slab, as shown in Figures 3(b) and 20(b).

6. Crack Propagation

6.1. Mixed-Mode Fracture Criterion. In order to clarify the propagation mechanism of track slab crack, the mixed-mode fracture criterion was selected to predict the propagation direction of track slab crack by considering the combined effect of tensile and shear stresses. The previous studies have shown that the maximum circumferential tensile stress criterion is in good agreement with the test data of brittle materials such as concrete and rock. Therefore, this criterion is often used to analyze the fracture mechanism of concrete structures. For the mixed-mode crack, the equivalent stress

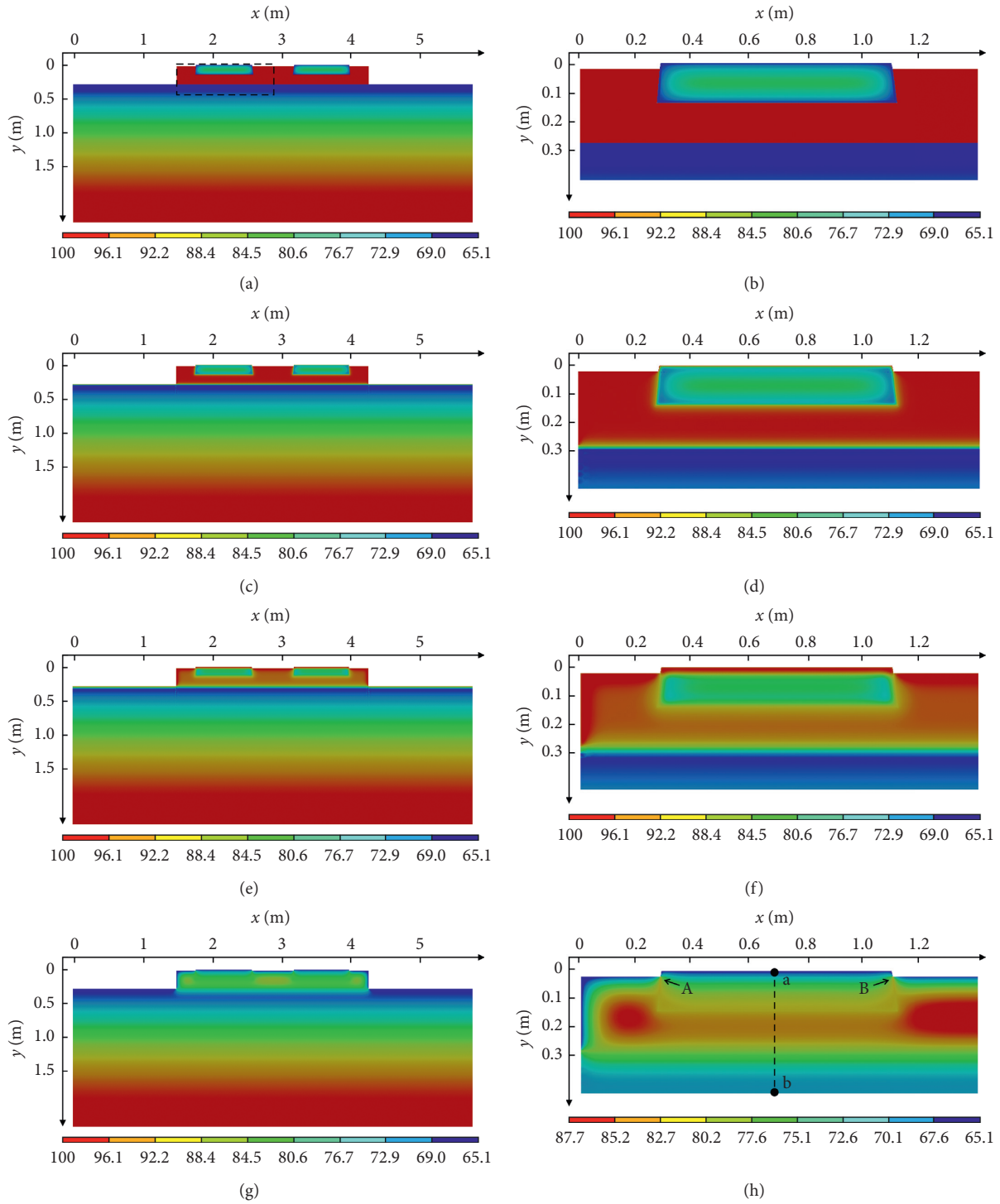

FIGURE 17: RH contour of ballastless track at different times. (a) $t = 0$ d, entire contour; (b) $t = 0$ d, local contour; (c) $t = 1$ d, entire contour; (d) $t = 1$ d, local contour; (e) $t = 7$ d, entire contour; (f) $t = 7$ d, local contour; (g) $t = 60$ d, entire contour; (h) $t = 60$ d, local contour.

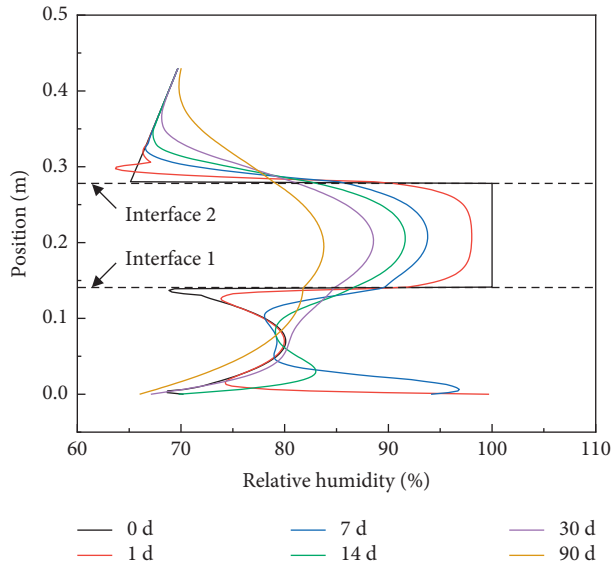

Figure 18: Distribution of RH along the path ab.

intensity factor K_{eff} can be evaluated by the following equation [31]:

$$K_{eff} = \sqrt{(K_{\text{I}} + K_{\text{II}})^2 + \frac{1}{1-2v}K_{\text{III}}^2}, \tag{13}$$

where v is Poisson's ratio and K_{I}, K_{II}, and K_{III} are the stress intensity factors in modes I, II, and III, respectively, which can be computed based on the displacement extrapolation method [32]; that is,

$$\begin{cases} K_{\text{I}} = \dfrac{G(v_c - v_e)}{\kappa + 1}\sqrt{\dfrac{2\pi}{r}}, \\ K_{\text{II}} = \dfrac{G(u_c - u_e)}{\kappa + 1}\sqrt{\dfrac{2\pi}{r}}, \\ K_{\text{III}} = \dfrac{G(w_c - w_e)}{\kappa + 1}\sqrt{\dfrac{2\pi}{r}}. \end{cases} \tag{14}$$

G is the shear modulus, κ is the coefficient related to Poisson's ratio, r is the element length, and u, v, and w are the node displacements in the x, y, and z directions, respectively, as shown in Figure 21.

When the equivalent stress intensity factor K_{eff} exceeds the fracture toughness K_{C}, the crack will lose the stability and fracture rapidly. The fracture condition can be expressed as

$$K_{\text{eff}} \geq K_{\text{C}}. \tag{15}$$

The maximum circumferential tensile stress criterion assumes that the crack propagates along the direction of the maximum circumferential tensile stress [33]:

$$\theta = 2\tan^{-1}\left[\frac{1}{4}\frac{K_{\text{I}}}{K_{\text{II}}} + \frac{1}{4}\sqrt{\left(\frac{K_{\text{I}}}{K_{\text{II}}}\right)^2 + 8}\right], \tag{16}$$

where θ is the turning angle of the crack, as shown in Figure 21.

The fracture models described above have been implemented in the ANSYS Workbench 18.0, and the flowchart of numerical procedure for the fatigue crack growth simulation is shown in Figure 22.

6.2. Results and Analysis. Based on the maximum circumferential tensile stress criterion, the propagation path of crack with an initial length $L_{\text{in}} = 0.1$ m and angle $\theta_{\text{in}} = 45^\circ$ was predicted, as shown in Table 2 and Figure 23. The results show that, under the action of drying shrinkage deformation of early-age concrete, the initial crack tip is subject to the combined action of tensile and shear stresses. In this case, the initial crack belongs to a mixed-mode crack, and the ratio of K_{II} and K_{III} to K_{I} is 31.37% and 7.6%, respectively. Under the combined action of stress intensity factors including K_{I}, K_{II}, and K_{III}, the initial crack direction will turn an angle of 30.06°, as shown in Figure 23(b). After the propagation path of initial crack has been turned, the ratio of K_{II} to K_{I} drops to 1.34%, and then the crack propagation path further turns an angle of 1.53°, as shown in Figure 23(c). Due to the continuous turning of crack propagation path, the final propagation path tends to be along the transverse direction of track slab, and the corresponding failure mode gradually transforms from mixed-model into pure opening-mode. When there are initial cracks at the corner of adjacent sleepers, the cracks would be coalesced

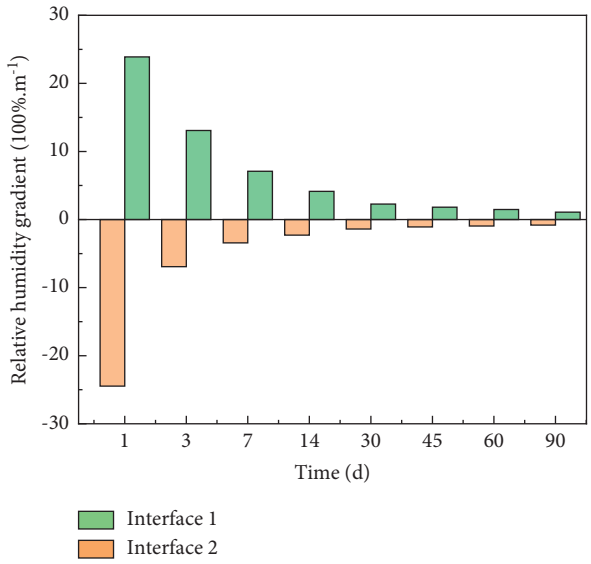

Figure 19: RHG at the interfaces.

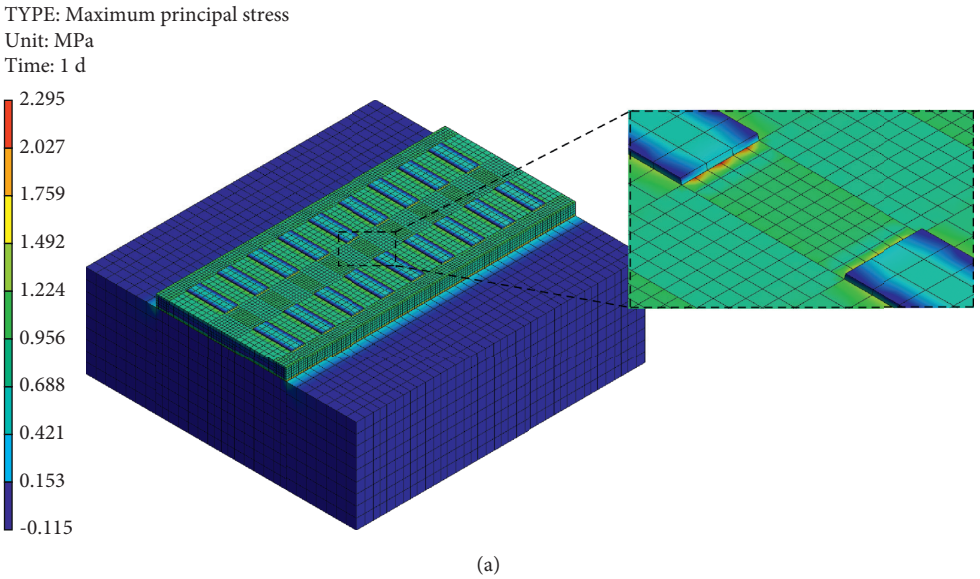

(a)

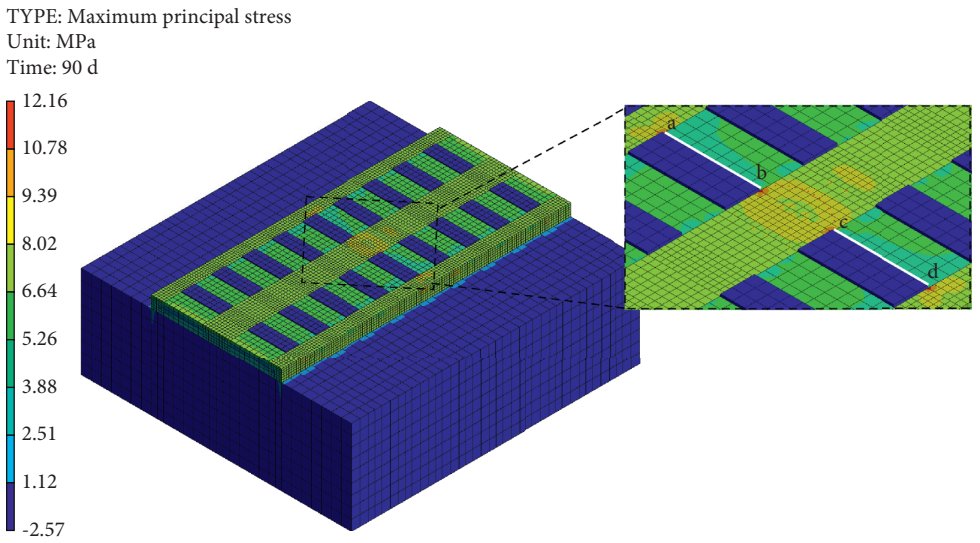

(b)

Figure 20: Maximum principal stress contour of ballastless track. (a) $t = 1$ d and (b) $t = 90$ d.

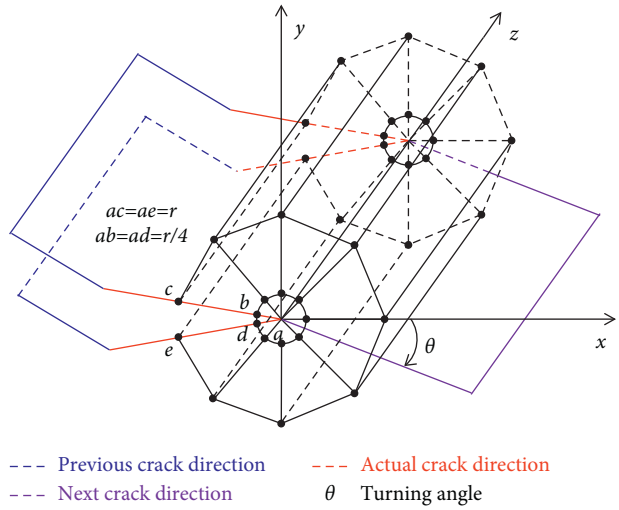

Figure 21: Singularity elements at the crack tip and crack propagation path.

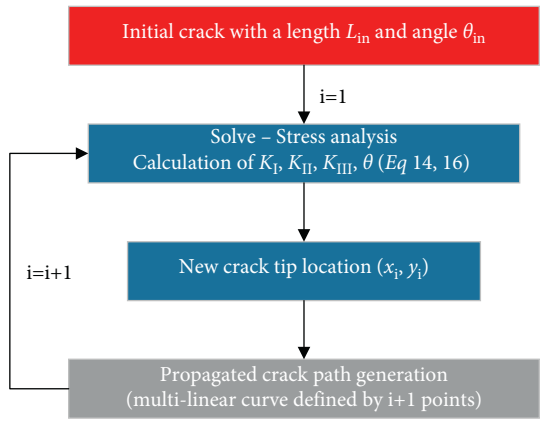

Figure 22: Numerical procedure for the fatigue crack growth simulation.

Table 2: Turning angle of the crack propagation path.

Crack length (m)	K_I (MPa.m$^{0.5}$)	K_{II} (MPa.m$^{0.5}$)	K_{III} (MPa.m$^{0.5}$)	K_{eff} (MPa.m$^{0.5}$)	Initial angle (°)	Previous angle (°)	Actural angle (°)	Turning angle (°)
0.1	3.8659	1.2128	0.2960	5.0930	45	—	45	30.06
0.2	5.2919	0.0709	0.0072	5.3637	45	45	14.94	1.53
0.3	5.4932	0.1268	0.0009	5.6200	45	14.94	13.41	2.65

and further form the transverse through-wall crack of track slab, as shown in Figures 3(b) and 23(d). The transverse through-wall crack not only significantly affects the comfortableness and safety of rapid transit railway, but also reduces the service life of ballastless track.

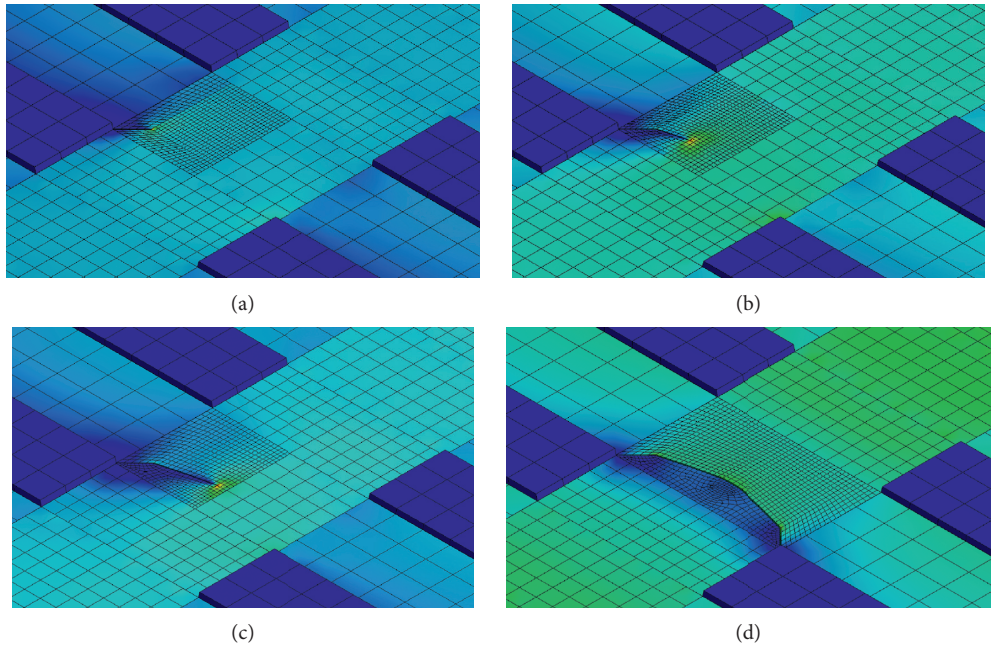

Figure 23: Predicted propagation paths of the crack with an initial angle of 45°. (a) $\theta = 30.06°$, (b) $\theta = 1.53°$, (c) $\theta = 2.65°$, and (d) crack coalescence.

7. Conclusions

This paper focuses on the drying-induced crack mechanism of the CRTS I bi-block ballastless track system induced by early-aged internal relative humidity. Considering the construction sequence and environmental conditions of the ballastless track system, the RH distribution in the system is simulated, and the crack propagation induced by the nonuniform RH is predicted. The following conclusions can be drawn:

(1) Under the long-term action of groundwater infiltration and external ambient air drying, the steady humidity of foundation along the depth obeys a cubic polynomial distribution. The steady result can provide an accurate initial humidity condition of foundation for the transient humidity field analysis of ballastless track relative to the linear interpolation method.

(2) After precasting the sleeper, the nonuniform humidity field is formed inside the sleeper. The surface relative humidity of sleeper is mainly affected by the ambient air drying, and the interior relative humidity is mainly controlled by the hydration self-desiccation. The transient result can provide a nonuniform initial humidity condition of sleepers for the transient humidity field analysis of ballastless track.

(3) After concreting the track slab in the site, the high humidity diffuses from track slab to sleepers and foundation through the bonded interfaces, and the maximum relative humidity gradient appears at the interface between track slab and sleeper. The maximum value rapidly decreases from $24.46 \times 100\%/m$ to $8.69 \times 100\%/m$ in the first week, and then the descending rate tends to be slow over time.

(4) Due to the drying shrinkage property of concrete materials, the stresses that occur at the interface between sleeper and track slab are greater than those at other areas. When the maximum principal stress exceeds the ultimate tensile strength of the track slab, the splayed crack with an initial angle of about 45° will be generated at the sleeper corner.

(5) Under the action of drying shrinkage deformation of early-age concrete, the initial splayed crack belongs to a mixed-mode crack, and the direction of crack tip turns an angle of 30.06°. Then, the final propagation path tends to be along the transverse direction of track slab due to the continuous turning of crack propagation path, and the corresponding failure mode gradually transforms from mixed-model into pure opening-mode. When there are initial cracks at the corner of adjacent sleepers, the cracks would be coalesced and further form the transverse through-wall crack of track slab. The transverse through-wall crack not only significantly affects the comfortableness and safety of rapid transit railway, but also reduces the service life of ballastless track.

Data Availability

All data used to support this study are available from the corresponding author upon reasonable request.

Conflicts of Interest

The authors declare that there are no conflicts of interest regarding the publication of this paper.

Acknowledgments

This project was supported by the National Natural Science Foundation of China (Grant nos. 51908197, 12072107, and 41907249), the Tackle Key Problems in Science and Technology Project of Henan Province, China (Grant no. 202102310262), the Key Research Project of Higher Education Institutions of Henan Province, China (Grant no. 20B580001), and Cultivation Programme for Young Backbone Teachers in Henan University of Technology (21420100).

References

[1] W. Zhai, K. Wang, Z. Chen, S. Zhu, C. Cai, and G. Liu, "Full-scale multi-functional test platform for investigating mechanical performance of track-subgrade systems of high-speed railways," *Railway Engineering Science*, vol. 28, no. 3, pp. 213–231, 2020.

[2] Q. Luo, M. Wei, Q. Lu, and W. Tengfei, "Simplified analytical solution for stress concentration ratio of piled embankments incorporating pile-soil interaction," *Railway Engineering Science*, vol. 29, no. 2, pp. 1–12, 2021.

[3] J. Zhu, H. Hu, Z. He, X. Guo, and W. Pan, "A power-quality monitoring and assessment system for high-speed railways based on train-network-data center integration," *Railway Engineering Science*, vol. 29, no. 1, pp. 30–41, 2021.

[4] X. Li, J. Ren, J. Wang, Y. Rongshan, S. Luhui, and L. Xueyi, "Drying shrinkage of early-age concrete for twin-block slab track," *Construction and Building Materials*, vol. 243, pp. 1–9, 2020.

[5] S. Yan, L. Ding, and S. Wang, "Key construction technology for CRTS I double-block ballastless track in tunnel," *Journal of Railway Engineering Society*, vol. 12, no. 11, pp. 13–16, 2009.

[6] R. Yang, J. Li, W. Kang, L. Xueyi, and C. Shihao, "Temperature characteristics analysis of the ballastless track under continuous hot weather," *Journal of Transportation Engineering, Part A: Systems*, vol. 143, no. 9, pp. 1–10, 2017.

[7] Z. Chen, J.-L. Xiao, X.-K. Liu, X.-Y. Liu, R.-S. Yang, and J.-J. Ren, "Effects of initial up-warp deformation on the stability of the CRTS II slab track at high temperatures," *Journal of Zhejiang University-Science*, vol. 19, no. 12, pp. 939–950, 2018.

[8] P. Zhao, C. Ding, L. Guo, Y. A. Zhang, and X. Liu, "A prototype fatigue test for slab track subjected to the coupling action of wheel load, temperature variation, and water erosion," *Proceedings of the Institution of Mechanical Engineers-Part F: Journal of Rail and Rapid Transit*, vol. 233, no. 5, pp. 566–579, 2019.

[9] S. Wang, R. Yang, X. Liu, P. Wang, and Z. Qian, "Discussion on ballastless track about the bring cause of crack and renovation measure," *Railway Engineering*, vol. 47, no. 9, pp. 76–79, 2007.

[10] Z. Zeng, Z. Huang, H. Yin, M. Xiaobai, W. Weidong, and W. Jundong, "Influence of track line environment on the temperature field of a double-block ballastless track slab," *Advances in Mechanical Engineering*, vol. 10, no. 12, pp. 1–16, 2018.

[11] S. Zhu, J. Luo, M. Wang, and C. Cai, "Mechanical characteristic variation of ballastless track in high-speed railway: effect of train-track interaction and environment loads," *Railway Engineering Science*, vol. 28, no. 4, pp. 408–423, 2020.

[12] D. Chen, "Multi-physical field coupling simulation of hygrothermal deformation of concrete," *Journal of Southeast University (Natural Science Edition)*, vol. 43, no. 3, pp. 582–587, 2013.

[13] Y. Han, J. Zhang, and Q. Yue, "Review on shrinkage of modern concrete," *Concrete*, vol. 29, no. 2, pp. 1–12, 2019.

[14] C. He, G. Miao, and X. Li, "Control measures for crack on ballastless track bed slab of plateau railway," *Railway Engineering*, vol. 61, no. 4, pp. 129–132, 2021.

[15] Y. Tan, Y. Zheng, and L. Kang, "Crack resistance performance of cast-in-situ concrete for double-block ballastless track," *Railway Engineering*, vol. 61, no. 2, pp. 91–94, 2021.

[16] J. Li, F. Xie, G. Zhao, and L. Li, "Experimental and numerical investigation of cast-in-situ concrete under external sulfate attack and drying-wetting cycles," *Construction and Building Materials*, vol. 249, Article ID 118789, 2020.

[17] P. Liu, W. Yu, W. Wang, and C. Ying, "Moisture transmission boundary condition between concrete and artificial simulation environment," *China Journal of Highway and Transport*, vol. 28, no. 5, pp. 108–116, 2015.

[18] H. Akita, T. Fujiwara, and Y. Ozaka, "A practical procedure for the analysis ofmoisture transfer within concrete due to drying," *Magazine of Concrete Research*, vol. 49, no. 179, pp. 129–137, 1997.

[19] L. J. Parrott, "Moisture profiles in drying concrete," *Advances in Cement Research*, vol. 1, no. 3, pp. 164–170, 1988.

[20] Y. Gao, "Studies on shrinkage and shrinkage induced stresses of concrete under dry-wet cycles," Dissertation, Tsinghua University, Beijing, China, 2013.

[21] J. Wang, H. Dai, and C. Gu, "Summary on numerical calculation of moisture transfer in concrete," *Journal of Hydroelectric Engineering*, vol. 24, no. 2, pp. 85–89, 2015.

[22] X. Gao and Y. Wei, "Modeling and analysis of moisture gradients in concrete pavements," *Engineering Mechanics*, vol. 31, no. 8, pp. 183–188, 2014.

[23] D. Shen, B. Zhou, M. Wang, Y. Chen, and G. Jiang, "Predicting relative humidity of early-age concrete under sealed and unsealed conditions," *Magazine of Concrete Research*, vol. 71, no. 22, pp. 1151–1166, 2019.

[24] Y. Wang, Y. Jia, and R. Zhao, "Calculation of internal humidity field of concrete based on ANSYS," *Journal of Southwest Jiaotong University*, vol. 52, no. 1, pp. 54–60, 2017.

[25] S. F. Wong, T. H. Wee, S. Swaddiwudhipong, and S. L. Lee, "Study of water movement in concrete," *Magazine of Concrete Research*, vol. 53, no. 3, pp. 205–220, 2001.

[26] W. Kang, S. Chen, and C. Wei, "Temperatures of ballastless track and effect of continuous hot weather," *Journal of the China Railway Society*, vol. 41, no. 7, pp. 127–134, 2019.

[27] Y. Wei, W. Hansen, J. J. Biernacki, and E. Schlangen, "Unified shrinkage model for concrete from autogenous shrinkage test on paste with and without ground-granulated blast-furnace slag," *ACI Materials Journal*, vol. 108, no. 1, pp. 13–20, 2011.

[28] G. Liu, "The mechanical analysis of CRST I Bi-block Track's process," Dissertation, Southwest Jiaotong University, Chengdu, China, 2015.

[29] J. H. Hattel and J. Thorborg, "A numerical model for predicting the thermomechanical conditions during hydration of early-age concrete," *Applied Mathematical Modelling*, vol. 27, no. 1, pp. 1–26, 2003.

[30] Y. Gao, J. Zhang, and D. Hou, "Calculation of moisture induced stresses and evaluation of crack risk in early-age concrete," *Engineering Mechanics*, vol. 29, no. 2, pp. 121–128, 2012.

[31] D. Xu and X. Fu, "Study on fracture criterion for I-II mixed mode crack by using four-point shearing specimen," *Journal of Hydraulic Engineering*, vol. 15, no. 9, pp. 63–69, 1984.
[32] J. M. Alegre and I. I. Cuesta, "Some aspects about the crack growth FEM simulations under mixed-mode loading," *International Journal of Fatigue*, vol. 32, no. 7, pp. 1090–1095, 2010.
[33] J. Li, "Experimental investigation on initial cracking criterion for I-II Mixed in concrete," Dissertation, Dalian University of Technology, Dalian, China, 2009.